CHEMISTRY OF MATERIALS

pubs.acs.org/cm

Article

Band Edge Energy Tuning through Electronic Character Hybridization in Ternary Metal Vanadates

Matthias H. Richter, Elizabeth A. Peterson, Lan Zhou, Aniketa A. Shinde, Paul F. Newhouse, Qimin Yan, Sean W. Fackler, Junko Yano, Jason K. Cooper, Kristin A. Persson, Jeffrey B. Neaton,* and John M. Gregoire*

Cite This: https://doi.org/10.1021/acs.chemmater.1c01415

Read Online

ACCESS | Metrics & More | Article Recommendations | Supporting Information

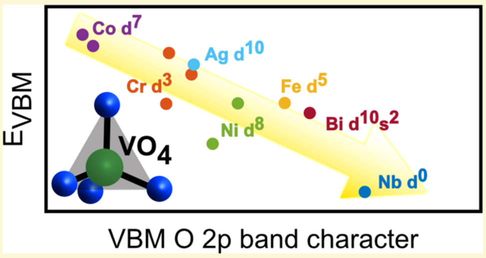

ABSTRACT: In the search for photoanode materials with band gaps suitable for utilization in solar fuel generation, approximately 1.2–2.8 eV, theory-guided experiments have identified a variety of materials that meet the band gap requirements and exhibit operational stability in harsh photoelectrochemical environments. In particular, M-V-O compounds (M is a transition metal or main group element) with VO_4 structural motifs were predicted to show a remarkably wide range of band energetics (>3 eV variation in the energy of valence band maximum) and characteristics, depending on the M and crystal structure, which is beyond the extent of electronic structured tuning observed in previously studied families of metal oxide photoanodes. While this finding guided experimental discovery of new photoanode materials, explicit experimental verification of the theoretical prediction of the tunable electronic structure of these materials has been lacking to date. In this study, we use X-ray photoelectron spectroscopy and Kelvin probe microscopy to experimentally investigate the electronic structure of M-V-O photoanodes, enabling comparison to theory on a common absolute energy scale. The results confirm the prediction that band edge energies of ternary vanadates vary significantly with metal cations. The valence band variation of approximately 1 eV observed here is larger than that reported in any analogous class of metal oxide semiconductors and demonstrates the promise of tuning the metal oxide electronic structure to enable efficient photoelectrocatalysis of the oxygen evolution reaction and beyond. Because midgap states can hamper realization of the high photovoltage sought by band edge tuning, we analyze the electronic contributions of oxygen vacancies for the representative photoanode $V_4Cr_2O_{13}$ to guide future research on the development of high-efficiency metal oxide photoanodes for solar fuel technology.

1. INTRODUCTION

The light-induced conversion of water and carbon dioxide into transportation fuels in integrated artificial photosynthesis structures is a promising alternative for a carbon neutral renewable energy economy.[1−6] Solar fuel generators use light to drive thermodynamically uphill reactions ($\Delta G > 0$) to store energy.[7] Integrated devices for solar fuel generation can be classified into several categories ranging from PV biased electrosynthetic cells (PV-electrolyzer) to photoelectrosynthetic cells.[8] For the former, light absorption and catalysis are fully separate entities that are governed by two different materials, whereas for the latter, light absorption and catalysis are driven by the same material in contact with the electrolyte. The challenge facing the discovery and development of suitable new materials for photoelectrosynthetic systems is the simultaneous realization of (1) a band gap suitable for solar absorption, (2) suitable band edge positions, and (3) operational stability in aqueous electrolytes.

A fully integrated cell for unassisted water splitting or CO_2 reduction (CO_2R) consists of anode and cathode sites for the oxygen evolution reaction (OER) and hydrogen evolution reaction (HER) or CO_2R, respectively. The minimum energy required to drive the reaction is determined by the energy difference between the thermodynamic potentials on the anode and cathode, for example, $E^0 = 1.23$ V for the OER/HER. This value and kinetic overpotentials determine the minimum required produced photovoltage (band gap) of the device. It can be achieved either by a single material (Janus material, single-photon process) or by combining two photosynthetic materials (two-photon process, Z-scheme), a photoanode and a photocathode, to reduce the band gap required to produce the necessary photoelectrochemical (PEC) potential. As energy is provided by converting photons into charge carriers, the available solar spectrum indicates that the combination of

Received: April 23, 2021
Revised: August 12, 2021

two light absorbers provides higher solar-to-fuel efficiency as the band gaps can be tailored toward the reactions.[9,10]

As photosynthetic materials not only absorb the light but also catalyze the anodic and/or cathodic reaction of the device, the position of the band edges, the valence band maximum (VBM) for photoanodes, and the conduction band minimum (CBM) for photocathodes need to be considered. On an absolute energy scale, the VBM is required to be lower in energy (higher in electric potential) than the anodic reaction (OER, E^0_{OER} = 1.23 V vs reversible hydrogen electrode (RHE)) and the CBM needs to be higher in energy than the cathodic reaction (e.g., HER, E^0_{HER} = 0.0 V vs RHE). Here, energy E and potential E follow the eq $\mathrm{E} = -q\cdot E$, that is, positive for states above the vacuum energy $\mathrm{E_{vac}}$ and negative energy for states below $\mathrm{E_{vac}}$. To align the energy levels of a solid (VBM and CBM) with electrochemical potentials of the reaction, two quantities need to be known: the standard half-cell potential with Nernst potential (activity of the species or their concentration)[11,12] and the absolute energy of the normal hydrogen electrode.[13] At pH = 0, a suitable photoanode must have a VBM of < −5.7 eV versus $\mathrm{E_{vac}}$ and a photocathode a CBM of > −4.5 eV versus $\mathrm{E_{vac}}$. For metal oxides, the positions of $\mathrm{E_{CBM}}$ and $\mathrm{E_{VBM}}$ generally follow a linear relation with pH (Nernst equation).[14,15] The Nernstian dependence indicates that the potential determining ions H^+ and/or OH^- are absorbed within the Helmholtz layer on the surface of the semiconductor forming a dipole. Hence, for metal oxides, the energetic position of $\mathrm{E_{CBM}}$ and $\mathrm{E_{VBM}}$ with respect to the RHE potential is constant.

A common point defect in metal oxides is an oxygen vacancy that can introduce in-gap states because of their creation of undercoordinated metal sites with a reduced oxidation state. The consequence is not only an increase in the n-type character of the oxide (as oxygen vacancies act as electron donors), which can increase electron conductivity, but also an increase in charge carrier recombination.[16,17] In conjunction with Fermi level pinning at the gap states, the turn-on potential is typically increased. For photoanodes, the turn-on potential is the lowest applied bias at which anodic photocurrent is still observed.

Band gap tuning and band edge tuning are most commonly studied in the context of multijunction solar cells based on III-V and II-VI semiconductors with a broad range of band gap and edge tuning enabling precise modification of the band gap of each subcell to maximize light harvesting efficiencies and achieve record conversion efficiencies.[18,19] For ternary alloys, the band gap is approximated with a quadratic dependence on the molar fraction of one component.[20] While this large extent of electronic structure tuning has been observed in select III-V and II-VI semiconductor systems via alloying, it is typically associated with lattice expansion and contraction.[21] The compositional and lattice constant variation with substitutional alloys is generally more limited in metal oxide systems, motivating our establishment of electronic structure tuning via systematic variation in the band edge character via electronic hybridization.

Alloying and cation substitution in metal oxides have been explored computationally for tuning band gap and band edge energies. For photocatalytic systems, TiO_2 has been in the center of attention, not only because of its catalytic properties[22] and sufficiently large band gap for unassisted operation, but also because of its ability to protect against corrosion.[23,24] Theoretical studies of TiO_2 focused, for example, on band position tuning by Se doping ($\Delta\mathrm{VBM_{DFT}}$ = 1.8 eV and $\Delta\mathrm{CBM_{DFT}}$ = ∼0.4 eV),[25] Ga doping ($\Delta\mathrm{VBM_{DFT}}$ = ∼0.6 eV and $\Delta\mathrm{CBM_{DFT}}$ = ∼0.9 eV),[26] or titanates with a hollandite structural motif ($\Delta\mathrm{VBM_{DFT}}$ = 1.1 eV and $\Delta\mathrm{CBM_{DFT}}$ = ∼0 eV) where the choice of cations also introduces shallow and deeper gap states.[27] Direct experimental verification of band edge positions for these systems is generally missing, limiting evaluation of whether broad band edge energy tunability can be realized and limiting its direct correlation with PEC performance.

A second material which has been in the strategic focus as a widely established photoanode material is $BiVO_4$.[28,29] Based on a common VO_4 structural motif between monoclinic $BiVO_4$ and other discovered photoanodes for the OER, α-Ag_3VO_4,[30] triclinic $FeVO_4$,[31,32] β-$Cu_3V_2O_8$,[33] and β-$Mn_2V_2O_7$,[34] a tiered screening workflow was previously implemented.[35] Therein, electronic structure calculations guided combinatorial synthesis and screening experiments to discover ternary metal vanadate photoanodes. The search space was defined as phases of type MO_x-VO_4 where VO_4 structural units are common among all materials and the MO_x motifs vary over a range of metal elements M. The intent was to identify the family of phases whose variation in the crystal structure and electronic configuration of M enables tuning of band edge positions to obtain (i) band gap energies in the visible spectrum for effective solar utilization and (ii) valence band (VB) energies higher than the typical metal oxide values of −6.5 to −7.5 eV versus $\mathrm{E_{vac}}$.[36] The subsequent computational prediction of >3 eV variation in the VBM position for various MO_x-VO_4 phases in the present work has no precedent with respect to those prior studies.[25−27] While those previous computational studies lack experimental validation of the predicted electronic structure tuning, we demonstrate realization of 1 eV variation in the band edge position.

The success in theoretical identification of visible gap MO_x-VO_4 metal oxides was experimentally validated through thin film synthesis of 15 phases and optical measurement of the band gap energy between 1.8 and 2.8 eV.[35] The variation in the band gap energy implies tunability of the band edge energies, and while theory in fact predicts such tunability, explicit verification via experimental measurement of band edge energies has been lacking to date.

In the present work, we combine X-ray photoelectron spectroscopy (XPS), Kelvin probe force microscopy (KPFM), and ultraviolet−visible (UV−vis) optical spectroscopy for the analysis of a set of 11 MO_x-VO_4 thin film materials prepared by physical vapor deposition to ascertain band energy tunability of ternary metal vanadates and compare it to the electronic structure computed with density functional theory (DFT). Theory and experiment are also combined to understand the energetics and orbital character of oxygen vacancy defects in $V_4Cr_2O_{13}$. In total, the results demonstrate the path for the development of high-efficiency, visible-gap metal oxide photoanodes through tuning of band edge positions and defect concentrations.

2. EXPERIMENTAL SECTION

The determination of electronic structure energetics in condensed matter by photoelectron spectroscopy is typically performed by combined core level and VB spectroscopy using XPS and ultraviolet photoemission spectroscopy (UPS), including the secondary electron emission cutoff, that is, work function measurements.[37] In addition to UPS, another approach to obtain information about the lateral distribution of the work function is KPFM. The latter is well suited for reproducible lateral work function screening of large composition libraries,[38] motivating our combination of XPS VB spectroscopy and KPFM to characterize band energetics.

2.1. X-ray Photoelectron Spectroscopy. XPS data were collected using a Kratos Axis Nova system with a base pressure of 1 × 10^{-9} Torr. The X-ray source was a monochromatic Al Kα line at 1486.6 eV. Photoelectrons were collected at 0° from the surface normal with a retarding pass energy of 160 eV for survey XPS scans with a step size of 0.5 eV and a pass energy of 40 eV for high-resolution VB scans with a step size of 0.05 eV. Where necessary, XPS data were collected using a small-spot mode lens mode with 110 μm aperture. The XPS data were calibrated using the Au $4f_{7/2}$ line (84 eV) of a sputter-cleaned gold foil. Repeated reference measurements of adventitious carbon on air-exposed gold showed a highly reproducible C 1 s binding energy of 285.0 eV with Au $4f_{7/2}$ at 84.0 eV. For the samples in this investigation, a C 1 s binding energy of less than or equal to 285 eV was observed indicating the absence of sample charging. No charge neutralization was used.

Data were analyzed using CasaXPS. To calculate the composition (atomic ratio), a Shirley background was subtracted. The core-level intensities were corrected by the analyzer transmission function and relative sensitivity factors to obtain corrected peak intensities, which were used to calculate the atomic ratios.

Resonant inelastic X-ray scattering (RiXS) experiments were performed at the Advanced Light Source, Berkeley at beamline 8.0.1, using the iRiXS end-station equipped with two slit-less variable line-spacing grating spectrographs with a resolution of ~0.3 eV.[39] X-ray absorption spectroscopy (XAS) data were collected in total electron yield mode and in total fluorescence yield mode. All data were normalized by the incident X-ray flux as measured by an Au mesh positioned upstream of the sample. Energies were calibrated using the XAS spectra of TiO_2 as a reference.

2.2. Kelvin Probe Force Microscopy. PeakForce KPFM data were collected using a Bruker Dimension Icon atomic force microscope. Bruker PFQNE-AL probes were used for the measurement. For each sample spot, several measurements of an area of 5 μm × 5 μm were taken. Each measurement consisted of a topographic, electrical (surface potential), and mechanical (adhesion, stiffness, and deformation) measurements. To reference the surface potential measurement (ϕ_{surface}, contact potential between the tip and sample) to a known standard, KPFM measurements of freshly exfoliated highly oriented pyrolytic graphite (HOPG) were performed prior to each sample. The contact potential difference (CPD) of a sample to HOPG could then be calculated using

$$\text{CPD}_{\text{sample}-\text{HOPG}} = \phi_{\text{surface, sample}} - \phi_{\text{surface,HOPG}} \quad (1)$$

The work function (ϕ) of the sample can then be calculated from the CPD by adding the known reference work function of HOPG (ϕ_{HOPG} = 4.6 eV) to the CPD.[38,40]

$$\phi_{\text{sample}} = q\cdot\text{CPD}_{\text{sample}-\text{HOPG}} + \phi_{\text{HOPG}} \quad (2)$$

2.3. Material Synthesis. The metal-vanadium (M-V) oxide composition libraries were fabricated using RF magnetron cosputtering onto 100 mm-diameter, 2.2 mm-thick glass substrates with a fluorine doped tin oxide (FTO) coating (Tec7, Hartford Glass Company) in a sputter deposition system (Kurt J. Lesker, CMS24) with 10^{-5} Pa base pressure. Cosputtering was performed using a V target and an additional metal target (M) except for the Ag-containing libraries, which used an Ag_2O target. The composition libraries were either deposited as "metal" or "oxide" thin films, referring to the absence or presence of reactive O_2 in the chamber and subjected to further annealing in air in a box oven.[35]

The crystal structures and phase distribution of the composition libraries were determined through X-ray diffraction (XRD) measurements on a Bruker Discover D8 XRD with a microfocus X-ray source (Cu) and a VÅNTEC-500 large microgap detector.

2.4. Theoretical Methods. The electronic structures of the ternary vanadates with a common VO_4 structural motif were computed via DFT as implemented in the Vienna ab initio simulation package.[41,42] Structural relaxations and terminal surface calculations were computed using the generalized gradient approximation as implemented by Perdew, Burke, and Ernzerhof (PBE)[43] in conjunction with Hubbard U values (PBE + U) using the Dudarev method.[44] Band structure and density of states (DOS) calculations for periodic structures were performed using the hybrid functional method developed by Heyd, Scuseria, and Ernzerhof (HSE).[45] A plane wave energy cutoff of 520 and 400 eV was used for PBE + U and HSE calculations, respectively. Recommended k-point grids and Hubbard U values taken from the Materials Project database[46] were used for each compound. The Hubbard U values used here have been shown to reproduce the formation enthalpies of transition metal oxides.[47] A somewhat smaller-than-typical mixing parameter of α = 0.17 was used for the DFT-HSE calculations, following prior work on the vanadates;[34,35] we used a standard screening parameter ω of 0.20. The relaxed geometries calculated with PBE + U are expected to compare well with those obtained with HSE. Indeed, prior first-principles calculations of metal oxides found that volumes optimized with HSE and PBE + U differ by about 5%.[35] The orbital character of the DOS of each oxide at the VB and CB edges was calculated by integrating the orbital-projected DOS at each band edge over a 0.5 eV energy range below and above the VB and CB, respectively, following the approach of ref 35.

In what follows, we also performed calculations of $V_4Cr_2O_{13}$ with an oxygen vacancy. We consider an 8.59 Å × 9.41 Å × 14.72 Å $V_4Cr_2O_{13}$ unit cell with a neutral oxygen vacancy, corresponding to a vacancy concentration of 1.3%. These systems were relaxed with PBE + U. Hubbard U_{eff} values of 3.25 and 3.7 eV were used for V and Cr, respectively. The partial density of states (pDOS) was then calculated with the HSE functional, with a mixing parameter of α = 0.17 and a screening parameter of ω of 0.20.

The defect formation energy was calculated using the expression

$$\text{E}^f[X^z] = \text{E}_{\text{tot}}[X^z] - \text{E}_{\text{tot}}[\text{bulk}] - \sum_i n_i\mu_i + z\,[\text{E}_{\text{F}} + \text{E}_{\text{VBM}}] + \Delta^z \quad (3)$$

where $\text{E}_{\text{tot}}[X^z]$ and $\text{E}_{\text{tot}}[\text{bulk}]$ are the total energy of the material containing defect X^z and the pristine bulk material, respectively; n_i is the change in the number of atoms of species i; μ_i is the chemical potential of species i; z is the charge state of defect X^z; E_{F} is the Fermi energy relative to the VB maximum (E_{VBM}); and Δ^z is a correction term to align the electrostatic potentials of the bulk and defect structures.[48] Because we consider a neutral defect in this work, the final two terms in eq 3 are unnecessary and neglected here. The chemical potential of oxygen was calculated following the approximation for an open system where entropy of oxygen and temperature dominate.[49−51]

3. RESULTS AND DISCUSSION

3.1. Validation of Band Edge Tuning Hypothesis. For the present work, 11 ternary vanadate metal oxides were considered. Figure 1a shows measurement of near-surface (XPS, see Figure S1 for raw spectra) and bulk (XRF) cation compositions compared to the FU. An off-stoichiometric XRF composition indicates that in the composition-spread thin film library, the highest phase purity of the target phase was observed at a slightly different composition from that of the FU. A difference in XPS and XRF compositions suggests some surface segregation of M or V, which could have occurred during synthesis or upon air exposure. While such composition deviations from the FU may alter the measured band energetics compared to the bulk values that would serve as the best comparison to theory, we show in Figure S2 that there is no evidence for systematic variation in band energy with XPS or XRF composition deviation. Phase identification from XRD patterns is illustrated in Figure S3 for each of the 11

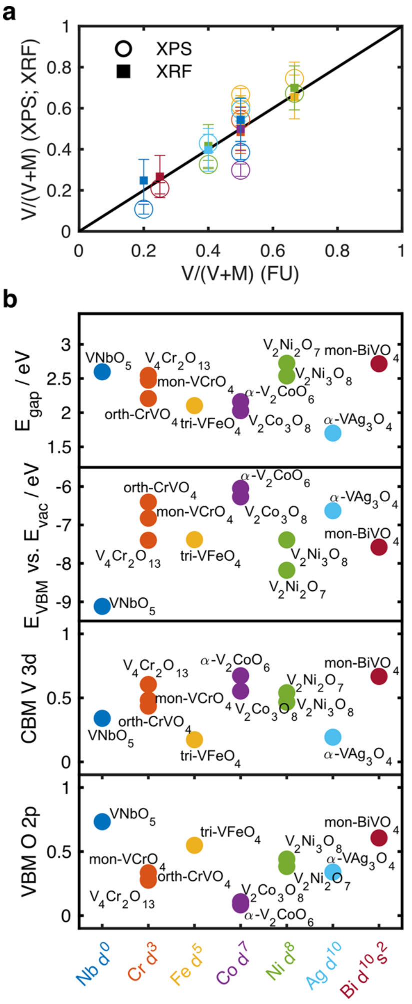

Figure 1. (a) XPS (open circles) and X-ray fluorescence (XRF) (solid squares) cation composition vs that of the formula unit (FU) of M-V-O compounds. The solid line represents the 1:1 relation. (b) Summary of predictions from DFT calculations for the VBM O 2p character, CBM V 3d character, VBM position, and band gap for different cations.[35] The color scheme of the cations is kept throughout all figures.

ternary M-V-O compounds. The only sample with an observable contaminant phase is $V_4Cr_2O_{13}$ that was synthesized by annealing a metallic Cr-V film, which resulted in ∼10% orth-$VCrO_4$ admixture. For the first part of this study to explore the band edge character-based tuning of band energetics, we exclude this sample as the $V_4Cr_2O_{13}$ phase was obtained with no observable contaminant phase by depositing an oxide film with subsequent annealing.

The 11 ternary vanadates are composed of seven different cations M, each with a distinct configuration, as indicated in Figure 1b. Nb $4d^0$ is the most similar to V, which is followed by a series of four first-row transition metals with nominal open d-shell configurations (Cr $3d^3$, Fe $3d^5$, Co $3d^7$, and Ni $3d^8$) and then a pair of cations with nominally filled d-shell configurations (Ag d^{10} and Bi $d^{10}s^2$). Exploring this breadth of electronic configurations was central to the photoanode discovery search strategy, as was the hypothesis that hybridization at and near the band edges of states introduced by these cations with V 3d and O 2p states would provide the desired variability in band edge energies. The V_2O_5 structure containing a network of VO_4 (with no additional cation) provides an excellent electronic template with the VB and CB of primarily O 2p and V 3d characters, respectively, and a band gap energy of 2.2 eV. Its VBM is near or below −7.2 eV versus E_{vac}, which is undesirably low,[52,53] motivating a focus on VB hybridization via addition of other cations into the structure. The calculated band characters, defined as the average contribution to the DOS within 0.5 eV of the respective band edge, VB energy, and band gap energy over the set of 11 structures are shown in Figure 1b. The 11 ternary vanadates exhibit a broad range of band characters, which in accordance with the above hypothesis, results in a substantial variation in the calculated DFT band edge energies.

Experimental validation of the variation in computed DFT band edge energy proceeded with XPS and KPFM, as shown in Figure 2, in addition to the previously reported band gap energies.[35] For each sample, an XPS overview (wide) scan and a VB spectrum were collected. All binding energies (E_B) are reported as negative values and referenced against the Fermi energy. To calculate the (surface) composition (Figure 1a), the wide scans have been used. The VBs of each of the M-V-O materials are shown in Figure 2a. By the intersection of a linear

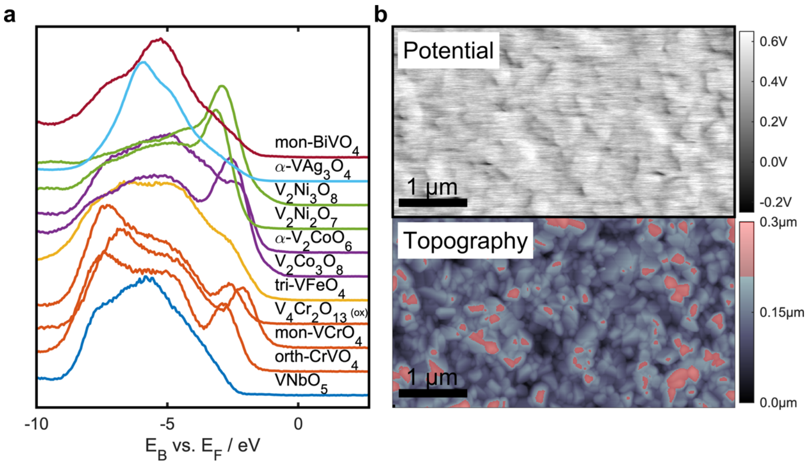

Figure 2. (a) XPS VB spectra of different M-V-O compounds. The binding energy is plotted against the Fermi energy. (b) Representative PeakForce KPFM images for topography and potential. The shaded red areas in (**b**, topography) mark the top 30% highest topographic areas for which the surface potential is extracted.

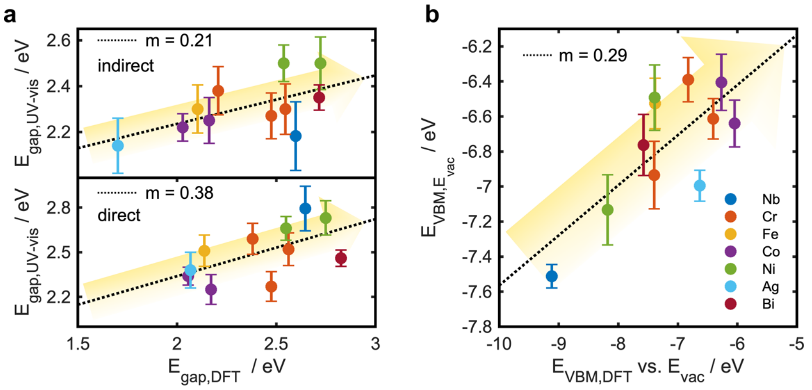

Figure 3. (a) Comparison of the experimental optical band gap to the band gap obtained from DFT-HSE calculation considering indirect-allowed (top) and direct-allowed (bottom) transitions. The correlation between both values (experiment and theory) is given by the slope ($m = 0.21$ for the indirect band gap and $m = 0.38$ for the direct band gap) of a least squares regression linear fit to the data (dashed line). (b) Comparison of experimental $E_{VBM,\ E_{vac}}$ to predicted $E_{VBM,\ DFT}$ position (DFT-PBE + U). The dashed line is a least squares regression linear fit with a slope of $m = 0.29$, illustrating the correlation between experiment and theory.

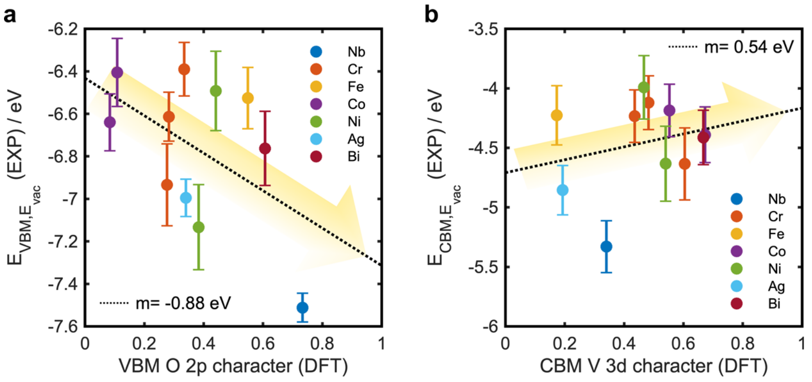

Figure 4. (a) Dependence of the experimental $E_{VBM,\ E_{vac}}$ position on the VBM O 2p character determined from our DFT calculations. The dashed line is linear fit to data with slope of $m = -0.88$ eV. (b) Dependence of the experimentally determined $E_{CBM,\ E_{vac}}$ position on the CBM V 3d character determined from our DFT calculations. The dashed line is linear fit to the data with a slope of $m = 0.54$ eV. The minimum optical band gap (indirect or direct absorption) was used in the calculation of the experimental CBM.

fit of the background to a linear fit to the onset of the VB spectrum, the position of the VBM was determined.

Additionally, the surface potential of each sample was determined by KPFM. Freshly exfoliated HOPG was used as a reference sample during KPFM measurements prior to each sample measurement to remove the influence of the KPFM tip potential. All surface potentials of the samples are reported herein as the CPD between HOPG and the respective M-V-O sample. The work function of each M-V-O sample was obtained by adding the work function of the reference sample (HOPG) to the CPD. A representative KPFM measurement is shown in Figure 2b. The bottom panel shows the topographic image of the area under investigation, whereas the top panel shows the lateral distribution of the surface potential at the same location. Topography and surface potentials were measured in parallel. Deep trenches in the sample increase the surface area surrounding the tip and thus the measured capacitance, creating an undesired morphology-dependent measurement and motivating the use of plateaus to measure and compare surface potential across the 11 structures. For each structure, the topography map was analyzed to extract the portions of the image within the top 30% of the maximum height, which mark the top plateaus of the topmost crystal particles. The mean and standard deviation of the corresponding set of KPFM measurements served as the value and uncertainty of the surface potential, respectively.

To approximate the energy of the CBM, the band gap determined by UV−vis spectroscopy (estimated uncertainty of ∼0.1 eV) was added to the experimentally obtained VBM position:

$$E_{CBM,E_F} = E_{VBM,E_F} + E_{gap,optical} \qquad (4)$$

Here, we neglect any contribution from exciton binding energies to the optical gap, expected to be of the order of 0.1 eV or less.[54−56] The subscript E_F implies that these values are references against the Fermi energy. Adding $CPD_{sample\text{-}HOPG}$ to these values produces band energies with respect to vacuum up to a constant offset. The vacuum-referenced VBM and CBM versus E_{vac} ($E_{VBM,\ E_{vac}}$ and $E_{CBM,\ E_{vac}}$) can be modeled by subtracting the work function of HOPG ($\phi_{HOPG} = 4.6$ eV).[40] The obtained $E_{VBM,\ E_{vac}}$ and $E_{CBM,\ E_{vac}}$ values could then be compared against predicted values obtained from DFT to establish the semiquantitative agreement among the ternary vanadates.

Figure 3a compares the calculated DFT-HSE band gaps with experimentally obtained optical band gaps. The values given here are in both cases the smallest calculated or measured gap, whether it is direct or indirect. In Figure 3b, a similar comparison is shown for calculated and experimentally determined positions of the VBM.

The mean absolute error for the indirect band gap trendline is 0.07 eV (Figure 3a top), for the direct band gap trendline, it is 0.11 eV (Figure 3a bottom), and for the VBM trendline, it is 0.19 eV (Figure 3b), each well within the expected accuracy of DFT calculations for these quantities for such systems. The qualitative trends are experimentally confirmed for both the band gap and VBM position. Quantitatively, the calculated variation in each band energy is larger than that observed experimentally, with linear regression between experimental and theoretical values indicating slopes of 0.21 for the indirect band gap, 0.38 for the direct band gap, and 0.29 for the VBM, each of which represents the fraction of the predicted variation that was experimentally realized.

To directly compare the influence of band edge tuning depending on the states introduced near the band edges by M in the M-V-O compounds, we compare experimental valence and conduction edge positions to the change in the O 2p or V 3d character of the respective band, as per the original hypothesis that these band character parameters would be key descriptors for the influence of M on the electronic structure. Figure 4 compares the measured $E_{\mathrm{VBM},\,E_{\mathrm{vac}}}$ and $E_{\mathrm{CBM},\,E_{\mathrm{vac}}}$ energies to the VBM O 2p and CBM V 3d character computed with DFT, respectively. The qualitative trends of increasing VBM energy with increasing O 2p character and of decreasing CBM energy with increasing V 3d affirm the hypothesis of band edge character-based tuning of band energetics. To quantitatively characterize these relationships, we summarize the comparison of experiment and theory using: (i) the slope of the least squares regression fit to the data, (ii) the Pearson correlation coefficient, and (iii) the confidence that the correlation has the respective sign. Regarding (i), the slopes of −0.88 and 0.54 eV per unit of band character, respectively, suggest that the band edges for ternary vanadates can be considerably tuned upon realization of phases that support a range of band characters. With the additional deviations of experimental VBM energies with respect to the trend line, $E_{\mathrm{VBM},\,E_{\mathrm{vac}}}$ can be tuned from −6.43 eV ± 0.11 eV to −7.31 eV ± 0.16 eV. To our knowledge, this dynamic range in band edge tuning has been neither proposed nor realized for a given class of materials of comparable scope as ternary metal vanadates with VO_4 structural motifs.

Descriptors (ii) and (iii) provide context for the substantial experimental uncertainty in the band edge energies. Regarding descriptor (ii), the correlation coefficients of −0.46 and 0.29, respectively, are consistent with the predictions that decreasing the O 2p band character will increase VBM energy and decreasing the V 3d band character will decrease CBM energy. Regarding descriptor (iii), the confidence of the negativity of the correlation between the O 2p band character and VBM energy is 89%, demonstrating high confidence in experimental validation of the theory-based hypothesis of VBM tuning via electronic hybridization. The corresponding confidence for positivity of the V 3d and CBM relationship is 65%. The lower absolute slope and correlation coefficient for this relationship compared to O 2p with the VBM are intuitive given that both the V 3d states and the states introduced by the M atom are d-electron states whose hybridization may be less consequential as the CBM has a predominant metal d character. The lower confidence in the existence of the predicted correlation for CBM position tuning is compounded by the propagation of error from three sources (XPS, KPFM, and UV−vis spectroscopy) for the CBM against two sources (XPS and XPFM) for the VBM in the experimental values.

3.2. Characterization of Defect States. Verification of the broad tunability of band edge positions sets the stage for identification of the optimal VB energy for visible-gap photoanodes to provide sufficiently energetic photogenerated holes for driving the OER while maintaining a sufficiently high photovoltage to couple with a visible-gap photocathode to drive solar fuel synthesis. A minimum requirement for developing a compatible photocathode and photoanode is that the turn-on potential for the photoanode must be lower than that of the photocathode so that in combination they can perform the anodic and cathodic reactions, respectively, without external bias. A primary hurdle to realize the low turn-on potential that is sought from band edge tuning is the presence of midgap states that limit quasi-Fermi level splitting by pinning the Fermi level over a range of potential and/or introducing carrier recombination pathways.[57,58] These undesirable states are often introduced by point defects, whose prevalence can vary considerably with synthesis conditions, motivating the study of defects and their electronic structure contributions to guide further material development.

To identify a representative system for the study of defects in ternary vanadates with extensive electronic hybridization, Cr and Co ternary vanadates are of interest because they exhibit the lowest O 2p VB character and thus highest VBM positions. Of these, $V_4Cr_2O_{13}$ exhibited the highest photocurrent in initial screening experiments (Figure S4),[35] motivating its selection for study herein.

Figure 5 shows the toggled-illumination cyclic voltammograms for $V_4Cr_2O_{13}$ photoanodes synthesized by different routes. While synthesis was conducted with 610 °C annealing in air for both samples, one electrode was sputter-deposited as a metal alloy ("metal-deposited)" while the other was the result of reactive sputtering to incorporate oxygen throughout the film prior to annealing ("oxide-deposited)". The oxide-deposited sample exhibits no photoactivity, whereas the metal-deposited film exhibits anodic photocurrent down to its terminal potential of 0.73 V versus RHE, 0.5 V below the OER Nernstian potential. Near this potential, a dark cathodic

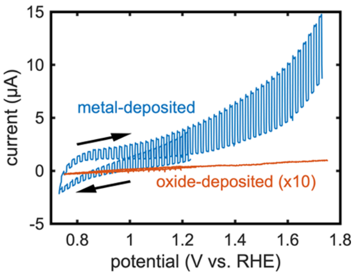

Figure 5. Toggled illumination cyclic voltammograms in pH 9 electrolyte for a pair of $V_4Cr_2O_{13}$ thin films deposited as Cr-V metal and then oxidized in air ("metal-deposited)" and deposited as an oxide thin film with subsequent annealing in air ("oxide-deposited)". The metal-deposited film exhibits anodic photocurrent in each illumination cycle across the entire potential range, whereas the oxide-deposited sample, whose current is scaled 10× in the figure, shows miniscule current transients upon illumination but otherwise is apparently an insulating film with negligible dark and photocurrents. The illumination is from a 385 nm light-emitting diode, and the illumination area is approximately 1 mm^2.

reaction, likely electrochemical reduction of Cr^{+3} and/or V^{+5}, obscures characterization of the photoanodic turn-on potential. Assuming that the overpotential for the OER is in excess of 0.3 V, these results suggest a quasi-Fermi level splitting in excess of 0.8 V but well below the 2.3 eV band gap. Given that the synthesis from a metal film may result in incomplete oxidation, oxygen vacancies are a likely source of point defects, motivating a computational study of such defects followed by experimental characterization of both electrodes from Figure 5.

With oxygen vacancies (V_O) comprising the most ubiquitous point defect for metal oxides,[59] and to assess whether such point defects would introduce midgap states, we consider a $V_4Cr_2O_{13}$ unit cell with a neutral oxygen vacancy concentration of 1.3 FU% or 1.9% of the defect-free O sites. The unit cell of $V_4Cr_2O_{13}$ is particularly large (76 atoms) and can accommodate a defect without the need for a larger supercell. The oxygen vacancy is selected to neighbor a Cr atom, and this choice of vacancy location is reasonable given the dominance of defect-related Cr d-d transitions over the respective V and O transitions in the RiXS data (intensity normalized to the elastic channel). The calculated PBE + U magnetic moments of Cr, V, and O in the pristine unit cell are 2.8, 0.1, and 0.03 μ_B, respectively. Upon introducing a neutral oxygen vacancy, the magnetic moment of the Cr and V nearest to the vacancy is modified to 3.4 and −0.8 μ_B, respectively, indicating both vacancy-induced alterations to the charge states and charge localization. The DFT-PBE formation energy of neutral oxygen vacancies at the experimental temperatures and partial pressures is shown in Figure S5. For annealing at 610 °C in air, we find 2.38 eV per 75 atom unit cell containing a single oxygen vacancy or 0.596 eV/FU. Charged oxygen vacancies can occur with lower formation energies in metal oxides as well, especially when the Fermi energy is closer to the VBM.[60−63] In our sample, we observed slight n-type behavior indicating that the Fermi energy is more likely to be closer to the CBM where neutral oxygen vacancies tend to be more stable. While we do not know for certain whether oxygen vacancies in our sample would be charged, we can say that the calculated defect formation energy sets an upper bound on the formation of either charged or neutral oxygen vacancies in this material.

The formation energy of both charged and neutral defects depends on the chemical potential of the added/removed species.[64] For ZnO, the absolute formation energy is 3.72 eV (0.08 eV/FU) for a neutral V_O,[65] 1.94−3.84 eV (0.12−0.24 eV/FU) for $FeWO_4$,[66] 2.02−4.9 eV (0.12−0.31 eV/FU) for $MnWO_4$,[66] 6.72 eV (0.09 eV/FU) for SiO_2,[67] and 5.2−6.6 eV (0.08−0.83 eV/FU) for TiO_2.[68]

To assess the electronic structure of neutral oxygen vacancies, the DOS of a unit cell (see the Supporting Information for details) with an oxygen vacancy from our DFT-HSE calculations was compared to the DOS of a defect-free structure, as shown in Figure 6a. To compare with the computed electronic structures, Figure 6b contains XPS VB spectra for $V_4Cr_2O_{13}$ synthesized by two routes: [i] deposited in an oxygen atmosphere and [ii] without oxygen present during deposition, both followed by reactive annealing in air. We hypothesize that the latter synthesis route is more susceptible to oxygen vacancies because oxygen diffusion throughout the thin film may be kinetically limited during the air annealing, as we have documented for other ternary oxides.[69] The difference in the XPS spectra from the two synthesis routes indicates a higher level of midgap states near the VBM for the metal-deposited sample. The difference in the XPS spectra from the two synthesis routes indicates a higher level of midgap states near the VBM for the metal-deposited sample. To estimate the defect concentration in the $V_4Cr_2O_{13}$ film, we compare the density of midgap states between computation and experiment. We calculate the ratio of the number of occupied midgap states to the number of states within 0.5 eV of the VBM and find that the ratio is 0.2 from DFT and 0.3 from XPS, indicating that the oxygen vacancy concentration may be on the order of the 1.3 FU% used in the DFT model.

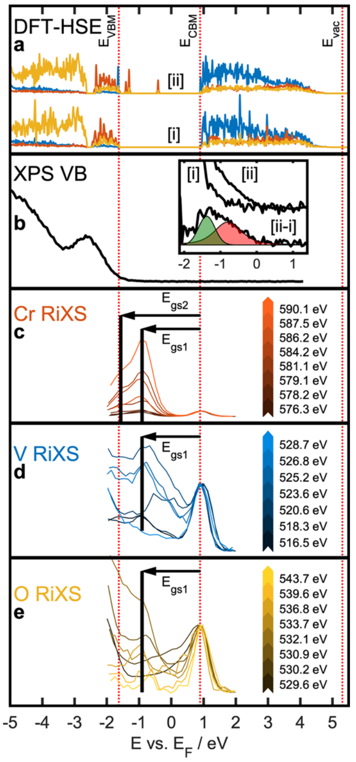

Figure 6. Direct comparison of defect states from DFT-HSE calculations and RiXS experiments. (a) pDOS from DFT-HSE [i] w/o oxygen vacancies and [ii] with oxygen vacancies, with pDOS associated with Cr (red), V (blue), and O (yellow) atoms indicated. (b) XPS ([i] oxide-deposited and [ii] metal-deposited) VB spectra with the inset showing the difference spectrum between the [ii] metal-deposited and [i] oxide-deposited $V_4Cr_2O_{13}$. Two gap states are evident in the difference spectra with a binding energy of −0.79 eV for $E_{B,gs1}$ (red) and −1.38 eV for $E_{B,gs2}$ (green). In the RiXS spectra for (c) Cr, (d) V, and (e) O, d-d transitions are visible for all three elements, demonstrating strong electronic hybridization. The Cr signals show two distinct transitions (E_{gs1} and E_{gs2}). The elastic channel for RiXS was aligned with the CBM. The position of E_{VBM}, E_{CBM}, and E_{vac} is indicated by vertical dotted red lines. The photon energy for each RiXS spectrum is given by the color-coded legend.

Characterization of the metal-deposited sample proceeded using RiXS to probe unoccupied states and transitions in the band gap region (Figure 6c−e). In Figure 6, the XPS binding energy versus Fermi energy was chosen as the common energy scale for all three characterization techniques. The DFT-HSE pDOS spectra were rigidly shifted to align the $E_{VBM,DFT}$ with $E_{VBM,XPS}$. The positions of E_{CBM} and E_{vac} were approximated by adding the direct optical absorption of 2.52 eV and ϕ from KPFM measurement of 5.31 eV to $E_{VBM,XPS}$, respectively. For

RiXS energy loss spectra, the energy adjustment was performed by aligning the elastic channel with E_{CBM}.

Comparing the pDOS in Figure 6a between the structures with and without oxygen vacancies shows two distinct differences: (i) a shift of the distribution of V 3d states in the VB and (ii) the appearance of two midgap states (GS). Our DFT results on the $V_4Cr_2O_{13}$ unit cell with a single neutral oxygen vacancy ($V_O = 8 \times 10^{20}$ cm^{-3}) show a slight absolute reduction of the DFT band gap by 0.14 eV (5% band gap reduction). The unit cell used for our DFT calculations is constructed so that neighboring oxygen vacancies are at least ~10 Å apart from each other to minimize interactions between periodic images and thereby to minimize dispersion in the midgap states. Prior literature has indicated that 10 Å of separation is generally sufficient for this purpose.[64] The sharpness of the midgap peaks indicates that this separation distance is sufficient for our discussion. In our calculations, we find that the vanadium VB states move closer to the VBM, although the average orbital contributions within 0.5 eV of the VBM and within 0.5 eV of the CBM are also not altered by the oxygen vacancy defect. Our DFT-HSE calculations suggest that oxygen vacancy defects introduce midgap states, whose relative energies with respect to E_{VBM} are computed to be 0.28 eV for GS2 and 1.25 eV for GS1 (Table S1). Both these values are larger than room-temperature thermal energy (0.026 eV), indicating that they likely do not act as donor or acceptor states impacting carrier concentration.

In both cases, the orbital character of the defect states is 70−80% Cr d and 15% O p, similar to that of the VB. The XPS spectra of Figure 6b are consistent with the presence of two primary types of midgap states in the metal-deposited $V_4Cr_2O_{13}$, as shown by the two-Gaussian fit to the difference spectrum. This fitting procedure indicates that the positions relative to E_{VBM} are 0.22 eV for GS2 and 0.81 eV for GS1 (Table S1), which are closer to the VBM than those predicted by DFT-HSE but in excellent qualitative agreement. Midgap states and charge carrier traps can be a result of surface hydroxide,[70] relative diffusion of the metal and oxygen atoms,[71] interstitials,[72] surface defects,[73] and reactivity of the material.[22] Although their absolute energy position can be different, the exact type of gap state is in several cases difficult to identify. While DFT-HSE provides an appropriate compromise of computational efficiency with adequate accuracy, the absolute defect energy level position in DFT will not only depend on the accuracy of the Kohn-Sham orbitals but also on the defect type, both of which could be explored further in future theoretical and experimental studies.[74,72]

XPS itself cannot reveal the elemental character of the VB or even the gap states. For this purpose, we employed resonant spectroscopy (RiXS) to obtain the required sensitivity. In particular, we used RiXS to investigate the presence and electronic character of gap states. The initial X-ray excitation of a Cr 2p or V 2p core level electron into an empty 3d CB state (e_g or t_{2g} in a crystal field) will create an excited electron ($3d^{n+1}$), which is strongly bound to the core hole and will not easily delocalize. A subsequent de-excitation process can occur via a decay of an electron from a 3d VB state (t_{2g} or e_g) into the core hole of the same atom. The final state will be an excited electron in a 3d CB state and a hole in a 3d VB state of the same transition metal element, that is, a d-d transition. Consequently, d-d transitions can only occur when 3d states are available in both the VB and CB, as has been extensively studied for early transition metals.[75−79] For pure $3d^0$ systems, defects among other things can facilitate local occupied 3d VB states allowing the observation of d-d transitions.[22] The process is depicted in Figure S6. Hybridization of O 2p and Cr 3d/V 3d states in the CB and VB excitation from the O 1 s core level into these hybridized states can also result in weak d-d transitions. The binding energy of O 1 s ($E_B = -530.5$ eV) is higher than that of V $2p_{3/2}$ ($E_B = -517.4$ eV) but lower than that of Cr $2p_{3/2}$ ($E_B = -577.6$ eV). Accordingly, only d-d transitions involving V are expected to result in substantial intensity in RiXS at the O K edge.

The RiXS spectra of metal-deposited $V_4Cr_2O_{13}$ in the vicinity of the elastic peak are shown in Figure 6c−e for Cr ($L_{2/3}$ edge), V ($L_{2/3}$ edge), and O (K edge), respectively. The elastic peak was aligned with E_{CBM} to account for the direction of the d-d transition (loss features). Comparing the spectra, we can observe that the intensity ratio of d-d transition to elastic peak is the highest for Cr and has a similar intensity and shape for V and O. This is in good agreement with HSE with a prediction of 70−80% Cr character. In the RiXS spectra for Cr (Figure 6c), two d-d transitions can be observed (labeled as E_{gs1} and E_{gs2}). The respective loss energy is 1.8 eV for $E_{gs1,CBM}$ and 2.4 eV for $E_{gs2,CBM}$ (energy with respect to the elastic peak, which is assumed to be the CBM). Using the optical band gap, we can then adjust the energy with respect to E_{VBM} and compare the values with the energy difference obtained by XPS. We obtain $E_{gs1,VBM} = 0.72$ eV and $E_{gs2,VBM} = 0.12$ eV, which is in good agreement with the energy difference obtained by XPS (0.81 and 0.22 eV, respectively, in Table S1). The complementary measurement of the energetic position of the midgap states by XPS and RiXS is in excellent agreement when using the direct optical absorption measured by UV−vis spectroscopy. The indirect gap is estimated to be 0.2 eV lower by UV−vis spectroscopy, which is within the uncertainty of the measurement because the indirect and direct absorption signals are not well separated. The calculated PBE + U values for the magnetic moment of Cr are 2.8 μ_B, close to the 3 μ_B that would be expected for octahedral crystal field splitting for Cr^{3+}.

This interpretation of the electronic structure and limiting photovoltage is consistent with all existing data, although as noted above, the electrochemical reduction of the metal oxide surface provides an additional limitation that may necessitate epitaxial films, or some other control of the spatial distribution of the surface, to accurately measure the flat band potential and more precisely compare the PEC attributes to the model of the defect electronic structure.

Collectively, this work demonstrates the utility of combined theory-experiment characterization of the electronic contributions of point defects to understand limitations and guide further material optimization of nascent metal oxide photoanodes. However, we conclude with evidence that the situation is even more complex than that indicated by Figure 6 and the ensuing comparison to experimental results. As noted above, the oxide-deposited sample exhibits a lower concentration of midgap states, which creates an expectation that its photovoltage may not be limited in the same manner as the metal-deposited sample. However, the oxide-deposited sample exhibits practically no photoresponse, creating a new question of whether the introduction of oxygen vacancies is somehow a prerequisite for photoactivity in which case one would conclude that this material is not amenable to development into a high-photovoltage semiconductor.

As the VB edge is dominated by states of localized Cr 3d character, small polarons may form and dominate carrier transport, limiting carrier mobilities.[80] Given the remarkably low dark current over the entire potential range in Figure 5, it appears that electronic conductivity may limit the performance of the oxide-deposited photoelectrode, which motivates future study of whether dopants, or defects other than oxygen vacancies, provide the mobile carriers that enable the photocurrent in the metal-deposited sample. In this case, photoanode optimization should proceed by developing a synthesis that results in the formation of those beneficial defects while mitigating oxygen vacancies.

The oxide-deposited and metal-deposited samples in Figures 5 and 6 were measured to have V cation concentration (see Figure 1a) of close to phase purity 0.66 using bulk-sensitive XRF. XPS showed a slightly V-rich surface composition with 0.75 and 0.7 for oxide- and metal-deposited $V_4Cr_2O_{13}$. While both values are within uncertainty of the FU composition, their differential composition indicates that the metal-deposited film has a higher concentration of V at the surface, although XRD characterization (Figure S3) indicates the presence of a small amount of the more Cr-rich phase, monoclinic $VCrO_4$. Although $VCrO_4$ can exhibit a 1 eV more positive VBM (DFT-HSE, Table S2), smaller band gap, and similar photoanodic performance,[35] a 10% impurity phase does not directly explain this performance difference between oxide and metal-deposited films, bringing into question whether cation substitutional or interstitial defects play a role in the electronic conductivity and/or doping level. A more detailed study on electronic transport as well as carrier dynamics and lifetime will be necessary to ascertain any positive influence of the oxygen vacancy-induced gap states on minority carrier transport properties. Additionally, fundamental understanding of charge carrier dynamics and limiting factors of these materials will lead to the development of new concepts to further improve their practical application as photoanodes, as has been shown for other ternary metal vanadates.[81,82]

4. CONCLUSIONS

XPS and Kelvin probe microscopy experiments for 11 ternary vanadate photoanodes provided characterization of the variation in band edge energetics with cation selection and crystal structure. The ternary vanadates collectively span seven different cations in structures that share a common VO_4 structural motif, which had been predicted to provide broad tunability of the VBM position via electronic hybridization of O 2p valence states and cationic valence states for metal oxide photoanodes. While the experimentally observed dynamic range of band positions was lower than that predicted, the qualitative trend was verified, providing the largest band edge tuning demonstrated to date for any analogous class of metal oxide semiconductors. The visible-gap photoanodes with a relatively high energy VB comprise the most promising electronic structures for a high-efficiency solar-driven OER, prompting further detailed characterization of the representative photoanode $V_4Cr_2O_{13}$. Our DFT-based predictions of midgap states arising from oxygen vacancy defects were supported by XPS and RiXS characterization, demonstrating that avoidance of these defects will be important for increasing the realizable photovoltage and ultimately high solar conversion efficiency.

■ ASSOCIATED CONTENT

Supporting Information

The Supporting Information is available free of charge at https://pubs.acs.org/doi/10.1021/acs.chemmater.1c01415.

> Supporting Information: XPS overview scans, XRD spectra and linear sweep voltammetry for all samples, formation energy of neutral oxygen vacancies, deviation of the experimental composition from FU, illustration of X-ray absorption and emission process, and tabulated theoretical and experimental data (PDF)

■ AUTHOR INFORMATION

Corresponding Authors

Jeffrey B. Neaton − *Department of Physics, University of California, Berkeley, California 94720, United States; Liquid Sunlight Alliance and Materials Sciences Division, Lawrence Berkeley National Laboratory, Berkeley, California 94720, United States; Kavli Energy NanoSciences Institute at Berkeley, Berkeley, California 94720, United States;* Email: jbneaton@lbl.gov

John M. Gregoire − *Division of Engineering and Applied Science and Liquid Sunlight Alliance, California Institute of Technology, Pasadena, California 91125, United States;* orcid.org/0000-0002-2863-5265; Email: gregoire@caltech.edu

Authors

Matthias H. Richter − *Division of Engineering and Applied Science and Liquid Sunlight Alliance, California Institute of Technology, Pasadena, California 91125, United States;* orcid.org/0000-0003-0091-2045

Elizabeth A. Peterson − *Department of Physics, University of California, Berkeley, California 94720, United States; Liquid Sunlight Alliance, Lawrence Berkeley National Laboratory, Berkeley, California 94720, United States;* orcid.org/0000-0001-5379-3604

Lan Zhou − *Division of Engineering and Applied Science and Liquid Sunlight Alliance, California Institute of Technology, Pasadena, California 91125, United States*

Aniketa A. Shinde − *Joint Center for Artificial Photosynthesis, California Institute of Technology, Pasadena, California 91125, United States;* orcid.org/0000-0003-2386-3848

Paul F. Newhouse − *Joint Center for Artificial Photosynthesis, California Institute of Technology, Pasadena, California 91125, United States*

Qimin Yan − *Department of Physics, University of California, Berkeley, California 94720, United States; Molecular Foundry, Lawrence Berkeley National Laboratory, Berkeley, California 94720, United States;* Present Address: Department of Physics, Temple University, Philadelphia, Pennsylvania 19122, United States (Q.Y.)

Sean W. Fackler − *Joint Center for Artificial Photosynthesis, Lawrence Berkeley National Laboratory, Berkeley, California 94720, United States*

Junko Yano − *Liquid Sunlight Alliance and Molecular Biophysics and Integrated Bioimaging Division, Lawrence Berkeley National Laboratory, Berkeley, California 94720, United States;* orcid.org/0000-0001-6308-9071

Jason K. Cooper − *Liquid Sunlight Alliance and Chemical Sciences Division, Lawrence Berkeley National Laboratory, Berkeley, California 94720, United States;* orcid.org/0000-0002-7953-4229

Kristin A. Persson − *Liquid Sunlight Alliance and Molecular Foundry, Lawrence Berkeley National Laboratory, Berkeley, California 94720, United States; Department of Materials Science and Engineering, University of California, Berkeley, California 94720, United States;* orcid.org/0000-0003-2495-5509

Complete contact information is available at:
https://pubs.acs.org/10.1021/acs.chemmater.1c01415

Notes

The authors declare no competing financial interest.

■ ACKNOWLEDGMENTS

The band character calculations and band energy experiments were supported by the Joint Center for Artificial Photosynthesis, a DOE Energy Innovation Hub, supported through the Office of Science of the US DOE (Award DE-SC0004993). Defect energy calculations and analysis of associated experimental data were supported by the Liquid Sunlight Alliance, which is supported by the U.S. Department of Energy, Office of Science, Office of Basic Energy Sciences, Fuels from Sunlight Hub under Award Number DE-SC0021266. Research was in part carried out at the Molecular Materials Research Center in the Beckman Institute of the California Institute of Technology. This research used resources of the Advanced Light Source, a U.S. DOE Office of Science User Facility under contract no. DE-AC02-05CH11231. We acknowledge computational resources provided by the National Energy Research Scientific Computing Center (NERSC), supported by the Office of Science of the Department of Energy under Award No. DE-AC02-05CH11231.

■ REFERENCES

(1) Kudo, A.; Miseki, Y. Heterogeneous Photocatalyst Materials for Water Splitting. *Chem. Soc. Rev.* **2009**, *38*, 253−278.

(2) Walter, M. G.; Warren, E. L.; McKone, J. R.; Boettcher, S. W.; Mi, Q.; Santori, E. A.; Lewis, N. S. Solar Water Splitting Cells. *Chem. Rev.* **2010**, *110*, 6446−6473.

(3) Fujishima, A.; Honda, K. Electrochemical Photolysis of Water at a Semiconductor Electrode. *Nature* **1972**, *238*, 37−38.

(4) Chu, S.; Li, W.; Yan, Y.; Hamann, T.; Shih, I.; Wang, D.; Mi, Z. Roadmap on Solar Water Splitting: Current Status and Future Prospects. *Nano Futures* **2017**, *1*, No. 022001.

(5) Mei, B.; Mul, G.; Seger, B. Beyond Water Splitting: Efficiencies of Photo-Electrochemical Devices Producing Hydrogen and Valuable Oxidation Products. *Adv. Sustain. Syst.* **2017**, *1*, No. 1600035.

(6) Hisatomi, T.; Domen, K. Introductory Lecture: Sunlight-Driven Water Splitting and Carbon Dioxide Reduction by Heterogeneous Semiconductor Systems as Key Processes in Artificial Photosynthesis. *Faraday Discuss.* **2017**, *198*, 11−35.

(7) Osterloh, F. E. Photocatalysis versus Photosynthesis: A Sensitivity Analysis of Devices for Solar Energy Conversion and Chemical Transformations. *ACS Energy Lett.* **2017**, *2*, 445−453.

(8) Nielander, A. C.; Shaner, M. R.; Papadantonakis, K. M.; Francis, S. A.; Lewis, N. S. A taxonomy for solar fuels generators. *Energy Environ. Sci.* **2015**, *8*, 16−25.

(9) Fountaine, K. T.; Lewerenz, H. J.; Atwater, H. A. Efficiency limits for photoelectrochemical water-splitting. *Nat. Commun.* **2016**, *7*, 13706.

(10) Gaudy, Y. K.; Gačević, Ž.; Haussener, S. Theoretical maximum photogeneration efficiency and performance characterization of $In_xGa_{1-x}N$/Si tandem water-splitting photoelectrodes. *APL Mater.* **2020**, *8*, No. 071111.

(11) Nernst, W. Zur Theorie umkehrbarer galvanischer Elemente. *Ber. Kgl. Pr. Akad. Wiss.* **1889**, 83−95.

(12) Nernst, W. Die elektromotorische Wirksamkeit der Jonen. *Z. Phys. Chem.* **1889**, *4U*, 129−181.

(13) Trasatti, S. The absolute electrode potential: an explanatory note (Recommendations 1986). *J. Electroanal. Chem. Interf. Electrochem.* **1986**, *209*, 417−428.

(14) Xu, Y.; Schoonen, M. A. A. The Absolute Energy Positions of Conduction and Valence Bands of Selected Semiconducting Minerals. *Am. Mineral.* **2000**, *85*, 543−556.

(15) Chen, S.; Wang, L.-W. Thermodynamic Oxidation and Reduction Potentials of Photocatalytic Semiconductors in Aqueous Solution. *Chem. Mater.* **2012**, *24*, 3659−3666.

(16) Kofstad, P. *Nonstoichiometry, Diffusion, and Electrical Conductivity in Binary Metal Oxides*; Wiley-Interscience: New York, 1972.

(17) Sze, S. M. *Physics of Semiconductor Devices*; Wiley Interscience: New York, 1981.

(18) Cariou, R.; Benick, J.; Feldmann, F.; Höhn, O.; Hauser, H.; Beutel, P.; Razek, N.; Wimplinger, M.; Bläsi, B.; Lackner, D.; Hermle, M.; Siefer, G.; Glunz, S. W.; Bett, A. W.; Dimroth, F. III−V-on-Silicon Solar Cells Reaching 33% Photoconversion Efficiency in Two-Terminal Configuration. *Nat. Energy* **2018**, *3*, 326−333.

(19) Geisz, J. F.; France, R. M.; Schulte, K. L.; Steiner, M. A.; Norman, A. G.; Guthrey, H. L.; Young, M. R.; Song; Moriarty, T. Six-Junction III−V Solar Cells With 47.1% Conversion Efficiency Under 143 Suns Concentration. *Nat. Energy* **2020**, *5*, 326−335.

(20) Van Vechten, J. A.; Bergstresser, T. K. Electronic Structures of Semiconductor Alloys. *Phys. Rev. B* **1970**, *1*, 3351−3358.

(21) Adachi, S. *Properties of Semiconductor Alloys: Group-IV, III-V and II-VI Semiconductors*; Wiley: Chichester, U.K., 2009.

(22) Diebold, U. The Surface Science of Titanium Dioxide. *Surf. Sci. Rep.* **2003**, *48*, 53−229.

(23) Hu, S.; Shaner, M. R.; Beardslee, J. A.; Lichterman, M.; Brunschwig, B. S.; Lewis, N. S. Amorphous TiO_2 coatings stabilize Si, GaAs, and GaP photoanodes for efficient water oxidation. *Science* **2014**, *344*, 1005−1009.

(24) Hu, S.; Richter, M. H.; Lichterman, M. F.; Beardslee, J.; Mayer, T.; Brunschwig, B. S.; Lewis, N. S. Electrical, Photoelectrochemical, and Photoelectron Spectroscopic Investigation of the Interfacial Transport and Energetics of Amorphous TiO_2/Si Heterojunctions. *J. Phys. Chem. C* **2016**, *120*, 3117−3129.

(25) Harb, M. New Insights Into the Origin of Visible-Light Photocatalytic Activity in Se-Modified Anatase TiO_2 From Screened Coulomb Hybrid DFT Calculations. *J. Phys. Chem. C* **2013**, *117*, 25229−25235.

(26) Fang, Y. Z.; Kong, X. J.; Wang, D. T.; Cui, S. X.; Liu, J. H. Role of Dopant Ga in Tuning the Band Gap of Rutile TiO_2 From First Principles. *Chin. J. Phys.* **2018**, *56*, 1370−1377.

(27) Moetakef, P.; Wang, L.; Maughan, A. E.; Gaskell, K. J.; Larson, A. M.; Hodges, B. C.; Rodriguez, E. E. Tuning the Electronic Band Structure of Microporous Titanates With the Hollandite Structure. *J. Mater. Chem. A* **2015**, *3*, 20330−20337.

(28) Kudo, A.; Omori, K.; Kato, H. A Novel Aqueous Process for Preparation of Crystal Form-Controlled and Highly Crystalline $BiVO_4$ Powder From Layered Vanadates at Room Temperature and Its Photocatalytic and Photophysical Properties. *J. Am. Chem. Soc.* **1999**, *121*, 11459−11467.

(29) Park, Y.; McDonald, K. J.; Choi, K.-S. Progress in Bismuth Vanadate Photoanodes for Use in Solar Water Oxidation. *Chem. Soc. Rev.* **2013**, *42*, 2321−2337.

(30) Chemelewski, W. D.; Mabayoje, O.; Mullins, C. B. SILAR Growth of Ag_3VO_4 and Characterization for Photoelectrochemical Water Oxidation. *J. Phys. Chem. C* **2015**, *119*, 26803−26808.

(31) Mandal, H.; Shyamal, S.; Hajra, P.; Bera, A.; Sariket, D.; Kundu, S.; Bhattacharya, C. Development of Ternary Iron Vanadium Oxide Semiconductors for Applications in Photoelectrochemical Water Oxidation. *RSC Adv.* **2016**, *6*, 4992−4999.

(32) Morton, C. D.; Slipper, I. J.; Thomas, M. J. K.; Alexander, B. D. Synthesis and Characterisation of Fe−V−O Thin Film Photoanodes. *J. Photochem. Photobiol. A: Chem.* **2010**, *216*, 209−214.

(33) Seabold, J. A.; Neale, N. R. All First Row Transition Metal Oxide Photoanode for Water Splitting Based on $Cu_3V_2O_8$. *Chem. Mater.* **2015**, *27*, 1005−1013.

(34) Yan, Q.; Li, G.; Newhouse, P. F.; Yu, J.; Persson, K. A.; Gregoire, J. M.; Neaton, J. B. $Mn_2V_2O_7$: An Earth Abundant Light Absorber for Solar Water Splitting. *Adv. Energy Mater.* **2015**, *5*, No. 1401840.

(35) Yan, Q.; Yu, J.; Suram, S. K.; Zhou, L.; Shinde, A.; Newhouse, P. F.; Chen, W.; Li, G.; Persson, K. A.; Gregoire, J. M.; Neaton, J. B. Solar fuels photoanode materials discovery by integrating high-throughput theory and experiment. *PNAS* **2017**, *114*, 3040−3043.

(36) Park, K.-W.; Kolpak, A. M. Optimal Methodology for Explicit Solvation Prediction of Band Edges of Transition Metal Oxide Photocatalysts. *Commun. Chem.* **2019**, *2*, 79.

(37) Mankel, E.; Hein, C.; Kühn, M.; Mayer, T. Electric potential distributions in space charge regions of molecular organic adsorbates using a simplified distributed states model. *Phys. Status Solidi A* **2014**, *211*, 2040−2048.

(38) Fernández Garrillo, A.; Grévin, B.; Chevalier, N.; Borowik, Ł. Calibrated work function mapping by Kelvin probe force microscopy. *Rev. Sci. Instrum.* **2018**, *89*, No. 043702.

(39) Qiao, R.; Li, Q.; Zhuo, Z.; Sallis, S.; Fuchs, O.; Blum, M.; Weinhardt, L.; Heske, C.; Pepper, J.; Jones, M.; Brown, A.; Spucces, A.; Chow, K.; Smith, B.; Glans, P.-A.; Chen, Y.; Yan, S.; Pan, F.; Piper, L. F. J.; Denlinger, J.; Guo, J.; Hussain, Z.; Chuang, Y. D.; Yang, W. High-efficiency in situ resonant inelastic x-ray scattering (iRIXS) endstation at the Advanced Light Source. *Rev. Sci. Instrum.* **2017**, *88*, No. 033106.

(40) Hansen, W. N.; Hansen, G. J. Standard reference surfaces for work function measurements in air. *Surf. Sci.* **2001**, *481*, 172−184.

(41) Kresse, G.; Furthmüller, J. Efficiency of Ab-Initio Total Energy Calculations for Metals and Semiconductors Using a Plane-Wave Basis Set. *Comput. Mater. Sci.* **1996**, *6*, 15−50.

(42) Kresse, G.; Furthmüller, J. Efficient Iterative Schemes for Ab Initio Total-Energy Calculations Using a Plane-Wave Basis Set. *Phys. Rev. B* **1996**, *54*, 11169−11186.

(43) Perdew, J. P.; Burke, K.; Ernzerhof, M. Generalized Gradient Approximation Made Simple. *Phys. Rev. Lett.* **1996**, *77*, 3865−3868.

(44) Dudarev, S. L.; Botton, G. A.; Savrasov, S. Y.; Humphreys, C. J.; Sutton, A. P. Electron-Energy-Loss Spectra and the Structural Stability of Nickel Oxide: An LSDA+U Study. *Phys. Rev. B* **1998**, *57*, 1505−1509.

(45) Heyd, J.; Scuseria, G. E.; Ernzerhof, M. Hybrid Functionals Based on a Screened Coulomb Potential. *J. Chem. Phys.* **2003**, *118*, 8207−8215.

(46) Jain, A.; Ong, S. P.; Hautier, G.; Chen, W.; Richards, W. D.; Dacek, S.; Cholia, S.; Gunter, D.; Skinner, D.; Ceder, G.; Persson, K. A. Commentary: The Materials Project: A Materials Genome Approach to Accelerating Materials Innovation. *APL Mater.* **2013**, *1*, No. 011002.

(47) Jain, A.; Hautier, G.; Ong, S. P.; Moore, C. J.; Fischer, C. C.; Persson, K. A.; Ceder, G. Formation Enthalpies by Mixing GGA and GGA+U Calculations. *Phys. Rev. B* **2011**, *84*, No. 045115.

(48) van de Walle, C. G.; Neugebauer, J. First-Principles Calculations for Defects and Impurities: Applications to III-Nitrides. *J. Appl. Phys.* **2004**, *95*, 3851−3879.

(49) Ong, S. P.; Wang, L.; Kang, B.; Ceder, G. Li-Fe-P-O_2 Phase Diagram From First Principles Calculations. *Chem. Mater.* **2008**, *20*, 1798−1807.

(50) Ong, S. P.; Jain, A.; Hautier, G.; Kang, B.; Ceder, G. Thermal Stabilities of Delithiated Olivine MPO_4 (M = Fe, Mn) Cathodes Investigated Using First Principles Calculations. *Electrochem. Commun.* **2010**, *12*, 427−430.

(51) *NIST-JANAF Thermochemical Tables.* https://janaf.nist.gov (accessed Feb 10, 2021).

(52) Aliaga, J.; Cifuentes, N.; González, G.; Sotomayor-Torres, C.; Benavente, E. Enhancement Photocatalytic Activity of the Heterojunction of Two-Dimensional Hybrid Semiconductors ZnO/V_2O_5. *Catalysts* **2018**, *8*, 374.

(53) Terán-Escobar, G.; Pampel, J.; Caicedo, J. M.; Lira-Cantú, M. Low-Temperature, Solution-Processed, Layered V_2O_5 Hydrate as the Hole-Transport Layer for Stable Organic Solar Cells. *Energy Environ. Sci.* **2013**, *6*, 3088−3098.

(54) Dvorak, M.; Wei, S.-H.; Wu, Z. Origin of the Variation of Exciton Binding Energy in Semiconductors. *Phys. Rev. Lett.* **2013**, *110*, No. 016402.

(55) Wiktor, J.; Reshetnyak, I.; Ambrosio, F.; Pasquarello, A. Comprehensive Modeling of the Band Gap and Absorption Spectrum Of $BiVO_4$. *Phys. Rev. Mater.* **2017**, *1*, No. 022401.

(56) Amtout, A.; Leonelli, R. Time-Resolved Photoluminescence From Excitons in TiO_2. *Solid State Commun.* **1992**, *84*, 349−352.

(57) Lichterman, M. F.; Hu, S.; Richter, M. H.; Crumlin, E. J.; Axnanda, S.; Favaro, M.; Drisdell, W.; Hussain, Z.; Mayer, T.; Brunschwig, B. S.; Lewis, N. S.; Liu, Z.; Lewerenz, H. J. Direct Observation of the Energetics at a Semiconductor/Liquid Junction by Operando X-Ray Photoelectron Spectroscopy. *Energy Environ. Sci.* **2015**, *8*, 2409−2416.

(58) Lichterman, M. F.; Richter, M. H.; Hu, S.; Crumlin, E. J.; Axnanda, S.; Favaro, M.; Drisdell, W.; Hussain, Z.; Brunschwig, B. S.; Lewis, N. S.; Liu, Z.; Lewerenz, H. J. An Electrochemical, Microtopographical and Ambient Pressure X-Ray Photoelectron Spectroscopic Investigation of Si/TiO_2/Ni/Electrolyte Interfaces. *J. Electrochem. Soc.* **2016**, *163*, H139−H146.

(59) Shluger, A. Defects in Oxides in Electronic Devices. In *Handbook of Materials Modeling: Applications: Current and Emerging Materials*; Andreoni, W., Yip, S., Eds.; Springer: Cham, 2018; 1−22.

(60) Tanaka, I.; Oba, F.; Tatsumi, K.; Kunisu, M.; Nakano, M.; Adachi, H. Theoretical Formation Energy of Oxygen-Vacancies in Oxides. *Mater. Trans.* **2002**, *43*, 1426−1429.

(61) Erhart, P.; Klein, A.; Albe, K. First-Principles Study of the Structure and Stability of Oxygen Defects in Zinc Oxide. *Phys. Rev. B* **2005**, *72*, No. 085213.

(62) Kamiya, K.; Yang, M. Y.; Magyari-Kope, B.; Niwa, M.; Nishi, Y.; Shiraishi, K. Vacancy Cohesion-Isolation Phase Transition Upon Charge Injection and Removal in Binary Oxide-Based RRAM Filamentary-Type Switching. *IEEE Trans. Electron Devices* **2013**, *60*, 3400−3406.

(63) Hashimoto, T.; Moriwake, H. Oxygen Vacancy Formation Energy and Its Effect on Spontaneous Polarization in $Bi_4Ti_3O_{12}$: A First-Principles Theoretical Study. *Phys. Rev. B* **2008**, *78*, No. 092106.

(64) Freysoldt, C.; Grabowski, B.; Hickel, T.; Neugebauer, J.; Kresse, G.; Janotti, A.; Van de Walle, C. G. First-Principles Calculations for Point Defects in Solids. *Rev. Mod. Phys.* **2014**, *86*, 253−305.

(65) Janotti, A.; Van de Walle, C. G. Native Point Defects in ZnO. *Phys. Rev. B* **2007**, *76*, No. 165202.

(66) Hoang, K. Polaron Formation, Native Defects, and Electronic Conduction in Metal Tungstates. *Phys. Rev. Mater.* **2017**, *1*, No. 024603.

(67) Yue, Y.; Song, Y.; Zuo, X. First Principles Study of Oxygen Vacancy Defects in Amorphous SiO_2. *AIP Adv.* **2017**, *7*, No. 015309.

(68) Elahifard, M.; Sadrian, M. R.; Mirzanejad, A.; Behjatmanesh-Ardakani, R.; Ahmadvand, S. Dispersion of Defects in TiO_2 Semiconductor: Oxygen Vacancies in the Bulk and Surface of Rutile and Anatase. *Catalysts* **2020**, *10*, 397.

(69) Zhou, L.; Shinde, A.; Suram, S. K.; Stein, H. S.; Bauers, S. R.; Zakutayev, A.; DuChene, J. S.; Liu, G.; Peterson, E. A.; Neaton, J. B.; Gregoire, J. M. Bi-Containing N-$FeWO_4$ Thin Films Provide the Largest Photovoltage and Highest Stability for a Sub-2 eV Band Gap Photoanode. *ACS Energy Lett.* **2018**, *3*, 2769−2774.

(70) Rothenberger, G.; Moser, J.; Graetzel, M.; Serpone, N.; Sharma, D. K. Charge Carrier Trapping and Recombination Dynamics in Small Semiconductor Particles. *J. Am. Chem. Soc.* **1985**, *107*, 8054−8059.

(71) Heitjans, P., Kärger, J., Eds. *Diffusion in Condensed Matter*; Springer: Berlin, Heidelberg, 2005.

(72) Wendt, S.; Sprunger, P. T.; Lira, E.; Madsen, G. K. H.; Li, Z.; Hansen, J. Ø.; Matthiesen, J.; Blekinge-Rasmussen, A.; Laegsgaard, E.; Hammer, B.; Besenbacher, F. The Role of Interstitial Sites in the Ti3d Defect State in the Band Gap of Titania. *Science* **2008**, *320*, 1755−1759.

(73) Liu, B.; Zhao, X.; Yu, J.; Parkin, I. P.; Fujishima, A.; Nakata, K. Intrinsic Intermediate Gap States of TiO_2 Materials and Their Roles in Charge Carrier Kinetics. *J. Photochem. Photobiol. C* **2019**, *39*, 1−57.

(74) Di Valentin, C.; Pacchioni, G.; Selloni, A. Reduced and n-Type Doped TiO_2: Nature of Ti^{3+} Species. *J. Phys. Chem. C* **2009**, *113*, 20543−20552.

(75) Agui, A.; Uozumi, T.; Mizumaki, M.; Kämbre, T. Intermetallic Charge Transfer in $FeTiO_3$ Probed by Resonant Inelastic Soft X-Ray Scattering. *Phys. Rev. B* **2009**, *79*, No. 092402.

(76) Harada, Y.; Kinugasa, T.; Eguchi, R.; Matsubara, M.; Kotani, A.; Watanabe, M.; Yagishita, A.; Shin, S. Polarization Dependence of Soft-X-Ray Raman Scattering at the L Edge of TiO_2. *Phys. Rev. B* **2000**, *61*, 12854−12859.

(77) Kurmaev, E. Z.; Moewes, A.; Butorin, S. M.; Katsnelson, M. I.; Finkelstein, L. D.; Nordgren, J.; Tedrow, P. M. Half-Metallic Electronic Structure of CrO_2 in Resonant Scattering. *Phys. Rev. B* **2003**, *67*, No. 155105.

(78) Zhang, G. P.; Callcott, T. A. Resolving dd Transitions in NaV_2O_5 Using Angle-Resolved Resonant Inelastic X-Ray Scattering at the V L Edge. *Phys. Rev. B* **2006**, *73*, 25102.

(79) Zhang, G. P.; Callcott, T. A.; Woods, G. T.; Lin, L.; Sales, B.; Mandrus, D.; He, J. Electron Correlation Effects in Resonant Inelastic X-Ray Scattering of NaV_2O_5. *Phys. Rev. Lett.* **2002**, *88*, No. 077401.

(80) Farrell, L.; Fleischer, K.; Caffrey, D.; Mullarkey, D.; Norton, E.; Shvets, I. V. Conducting Mechanism in the Epitaxial p-Type Transparent Conducting Oxide Cr_2O_3:Mg. *Phys. Rev. B* **2015**, *91*, No. 125202.

(81) Abdi, F. F.; van de Krol, R. Nature and Light Dependence of Bulk Recombination in Co-Pi-Catalyzed $BiVO_4$ Photoanodes. *J. Phys. Chem. C* **2012**, *116*, 9398−9404.

(82) Abdi, F. F.; Han, L.; Smets, A. H. M.; Zeman, M.; Dam, B.; van de Krol, R. Efficient Solar Water Splitting by Enhanced Charge Separation in a Bismuth Vanadate-Silicon Tandem Photoelectrode. *Nat. Commun.* **2013**, *4*, 2195.